Chapter 5

Consequences of Low-χ Block Polymer Design: Phase Behavior, Equilibrium, and Crystallization

ABSTRACT

The preceding chapter describes our discovery of an unusual partially mixed lamellar morphology (LAM$_P$) in LSO brush triblock terpolymers featuring grafted poly($_{D,L}$-lactide) (L), polystyrene (S), and poly(ethylene oxide) (O) side chains. Partial mixing emerges as a consequence of low-χ interactions between the end blocks. This chapter will describe other physical consequences associated with the molecular architecture and low-χ design. We will first discuss the ternary phase diagram for LSO brush triblock terpolymers, representing variations in both the relative backbone degrees of polymerization and the side chain molecular weights (Section 5-1). The influence of the brush architecture will be highlighted across >100 unique samples. Section 5-2 will address potential non-equilibrium effects in brush LSO, which may affect comparisons with theory. Variable-temperature X-ray scattering experiments indicate that LAM$_P$ is thermally stable: consistent with other reports of fully grafted bottlebrush polymers, no order-disorder transition is observed below the onset of decomposition. Lastly, Section 5-3 will discuss the crystallization of PEO in LSO brush triblock terpolymers, in particular highlighting trends in the crystal orientation with O block backbone length. The potential contributions of screening and confinement effects will be described. Collectively, these studies of the phase behavior of brush LSO and brush LS + X (where X = L, S, or O) provide key insights into the roles of the brush polymer architecture, chain connectivity, and molecular interactions. Understanding the complex interplay of these structural and chemical parameters introduces new guidelines for low-χ block polymer design.

Table of Contents

5-1 Ternary Phase Behavior

5-1.1 LSO Brush Triblock Terpolymers

Bottlebrush polymers adopt extended conformations compared to their linear analogues.[1-4] Steric interactions between the densely grafted side chains impart a certain bending rigidity to the backbone, which manifests in the strong scaling of domain sizes with total backbone length (Chapter 3-3), ultrahigh entanglement molecular weights (Chapter 3-4), and other physical phenomena. These architecture effects offer many advantages in the context of block polymer self-assembly, enabling the fabrication of structures with large domain sizes[5-7] and large grain sizes.[8] However, the relative bending rigidity also introduces one potential limitation: in general, densely grafted block polymers resist the interfacial curvature required to access non-lamellar morphologies. Brush diblock polymers with symmetric side chains exclusively self-assemble to 1D lamellar structures,[6,9] even at highly asymmetric compositions where analogous *linear* diblock polymers form 2D or 3D morphologies.[10-11]

Varying the molecular architecture can enable brush-like polymers to access non-lamellar morphologies: for example, cylinder, sphere, and gyroid phases have been recently identified for graft block polymers with asymmetric side chain lengths[9,12-15] or A-*branch*-B "Janus" architectures.[16] This section will describe another approach to modifying the chain connectivity: synthesizing **ABC** brush triblock terpolymers. Compared to AB diblock polymers, ABC triblock terpolymers vastly expand the parameter space for materials design. Whereas the phase behavior of AB diblock polymers can be captured by *three* independent parameters (the total degree of polymerization, N; the volume fraction of block A, $f_A = 1-f_B$;

and the free-energy penalty to mixing blocks, χ_{AB}) the phase behavior of ABC triblock terpolymers requires *six* parameters for complete description: N, f_A, f_B, χ_{AB}, χ_{BC}, and χ_{AC}.[11,17] A rich phase space emerges. Figure 5.1 provides select examples of the variety of morphologies identified for linear ABC triblock terpolymers.

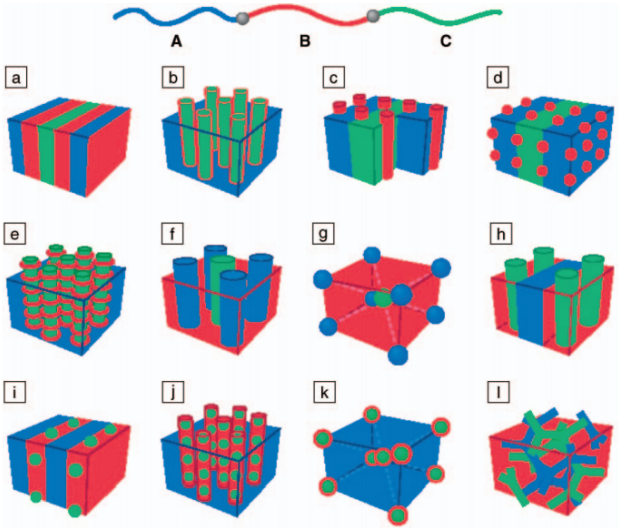

Figure 5.1: Schematic illustrations of the diverse morphologies identified for linear ABC triblock terpolymers. Variations in the block sequence and block volume fractions create an enormous parameter space for materials design. Reproduced with permission from Refs. 11 and 17.

The phase behavior of *linear* ABC triblock terpolymers has been extensively investigated through both theory[17-22] and experiments.[23-28] However, the phase behavior of *brush* ABC triblocks has not been systematically studied, in large part due to long-standing challenges associated with synthesizing well-defined materials. In this section, we present our work to close this gap. Bottlebrush triblock terpolymers with grafted poly(D,L-lactide) (L), polystyrene (S), and poly(ethylene oxide) (O) side chains were synthesized by living ring-opening metathesis polymerization (ROMP). (Further synthetic information can be found in Appendix C-2.) Sequential ROMP provides a robust, modular strategy to tune key elements of the molecular architecture (Scheme 5.1): (1) the block sequence (LSO, LOS, or LSO, via the order of addition), (2) the backbone degrees of polymerization (N_A, N_B, and N_C, via the equivalents of each macromonomer to the catalyst), and (3) the side chain degrees of polymerization (x, y, and z, via the macromonomer molecular weights). This extensive

synthetic tunability enables systematic studies of influence of molecular architecture on ABC brush triblock terpolymer self-assembly.

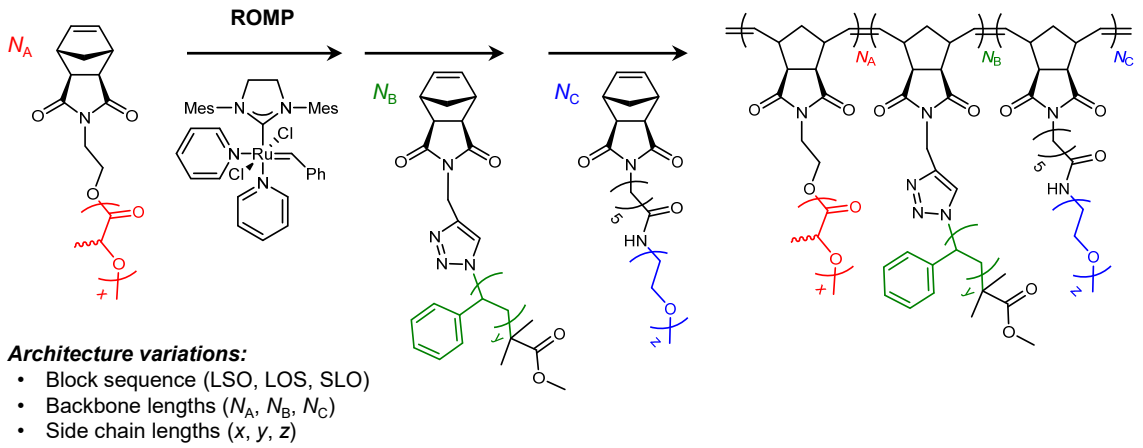

Scheme 5.1: Synthesis of LSO brush triblock terpolymers by ring-opening metathesis polymerization (ROMP). The block sequence, backbone lengths, and side chain lengths can be readily varied.

Scheme 5.1 presents the synthesis of brush LSO. The relative values of the three binary interaction parameters impose $\chi_{AB} > \chi_{BC} > \chi_{AC}$ (where $\chi_{AB} \equiv \chi_{LS}$, $\chi_{BC} \equiv \chi_{SO}$, and $\chi_{AC} \equiv \chi_{LO}$). This choice of block chemistry and sequence introduces morphological frustration. In this frustrated system, the highest-χ interactions occur between adjacent blocks (A/B and B/C). Chain connectivity requires adjacent blocks to share domain interfaces, but the large enthalpic penalties to mixing A/B and B/C segments instead favor the formation of A/C interfaces. Because the A and C blocks are not directly connected, accommodating A/C interfaces while minimizing A/B and B/C contacts favors the formation of 2D and 3D morphologies. Figure 5.2 presents the ternary phase diagram for reported *linear* ABC triblock terpolymers that experience the same type of morphological frustration as brush LSO. (Data were compiled for linear polystyrene-*b*-polybutadiene-*b*-poly(methyl methacrylate) (SBM)[24,29-32] and polystyrene-*b*-poly(ethylene-*co*-butadiene)-*b*-poly(methyl methacrylate [S(EB)M][23-24,32-34]). A rich variety of exotic morphologies emerge as a consequence of frustration, such as helices on spheres, core-shell cylinders, and knitting patterns.

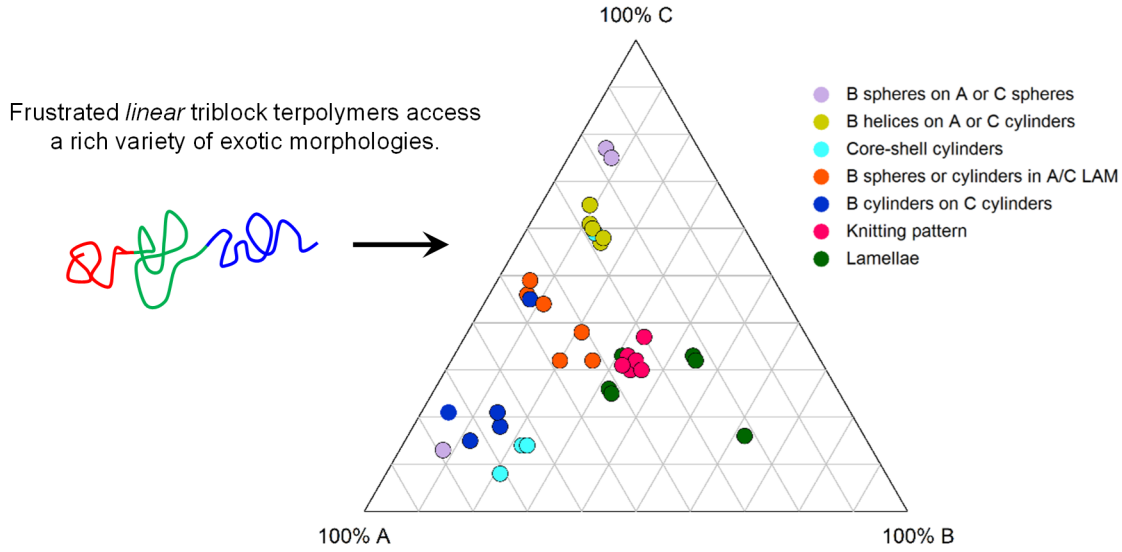

Figure 5.2: Ternary phase diagram for reported *linear* ABC triblock terpolymers with similar frustration (Type II) as LSO. The vertices each represent 100% pure A, B, or C by volume; moving away from a vertex in any direction represents decreasing the volume fraction of the corresponding component. The examples include linear PS-*b*-PB-*b*-PMMA and PS-*b*-P(E-*co*-B)-*b*-PMMA triblocks, compiled from Refs. 23–24 and 29–34.

Can densely grafted bottlebrush triblock terpolymers access similar morphologies? Previous work suggests that the increased bending rigidity of bottlebrush polymers relative to linear analogues strongly disfavors the interfacial curvature required by non-lamellar morphologies. In this context, potential conflicts between the molecular architecture and morphological frustration arise in LSO brush triblock terpolymers.

We synthesized >100 unique LSO brush triblock terpolymers via living ROMP (Scheme 5.1). The total backbone degree of polymerization was fixed (N_{bb} = 80), and the block volume fractions (f_A, f_B) were varied across the entire composition space. Unlike linear block polymers, brush block polymers feature two independent handles to tune the composition (*i.e.*, the backbone block lengths and side chain lengths). The brush LSO samples comprised five variations in the side chain molecular weights: [2-2-2], [2-2-3], [2-2-5], [5-2-2], and [5-2-3], where each [M_L, M_S, M_O] indicates the side chain molecular weight in kg/mol. All samples were annealed at 140 °C under modest applied pressure, and the ordered structures that developed were identified by synchrotron small-angle X-ray scattering (SAXS). (See Appendix C-6 for further SAXS information.)

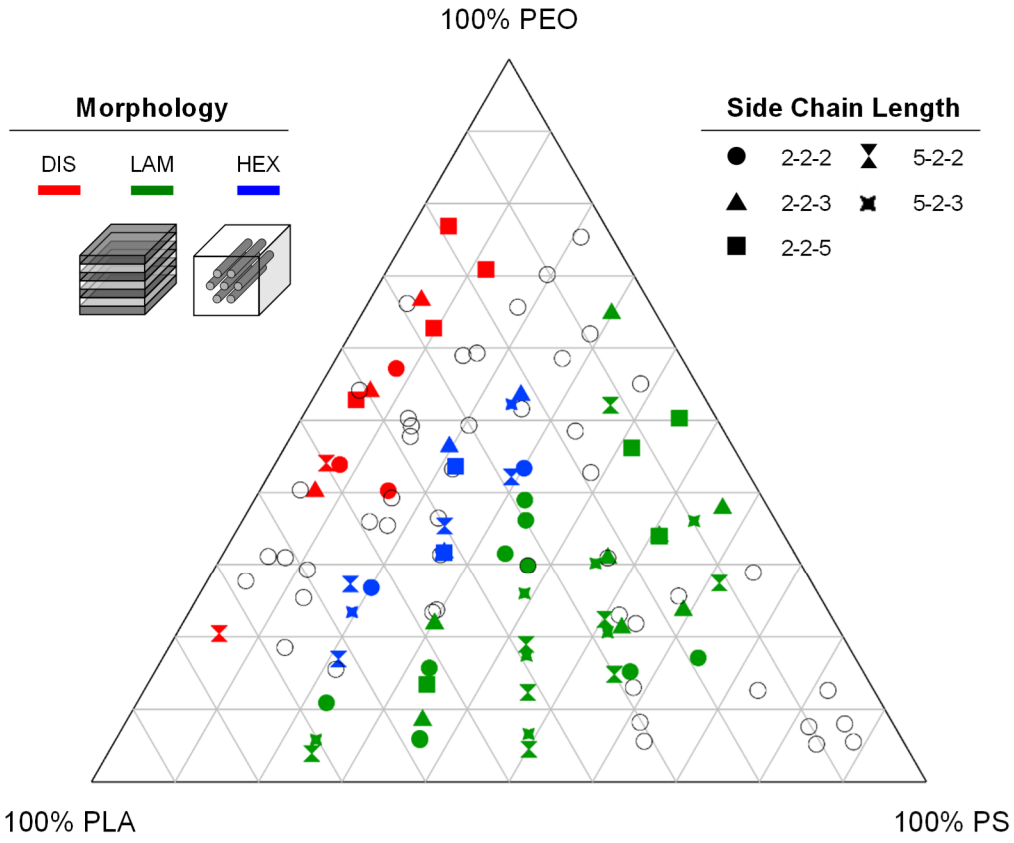

Figure 5.3: Ternary phase diagram for LSO brush triblock terpolymers. The vertices each represent 100% pure PLA (L), PS (S), or PEO (O) by volume. Each symbol represents a brush LSO triblock synthesized, annealed, and studied by SAXS. The colors indicate different morphologies: (*red*) disordered, (*green*) lamellar, (*blue*) hexagonally packed cylinders. The shapes indicate different side chain lengths: in the legend on the right, each triplet indicates [M_L, M_S, and M_O], where M_i is the number-average molecular weight (in kg/mol) of each side chain *i*. Unfilled symbols indicate samples that could not be unambiguously assigned by SAXS.

Figure 5.3 presents the ternary phase diagram for LSO brush triblock terpolymers. Colored symbols represent the different morphologies identified by SAXS, while unfilled symbols indicate samples that could not be unambiguously assigned. Different shapes indicate different combinations of side chain molecular weights. The assigned structures correlate with the composition, leading to narrow regions of disordered materials (DIS, $f_{PS} \approx 0$) and hexagonally packed cylinders (HEX, $f_{PS} \approx 0.25$) as well as a wide swath of lamellae (LAM, $f_{PS} > 0.25$).The phase behavior does not appear to be influenced by the way in which the composition is varied: that is, despite potential differences in the relative backbone lengths and/or side chain lengths, LSO brush triblock terpolymers with similar block volume

fractions assemble to the same morphology. This observation is perhaps surprising, since side chain length asymmetry strongly influences the phase behavior of brush *diblock* polymers.[9,12-15] Further increasing the side chain asymmetry may produce similar effects in brush LSO.

In contrast to linear ABC triblock terpolymers, for which a rich variety of morphologies are observed (Figures 5.1–5.2), the brush LSO triblock terpolymers studied herein only assemble to HEX or LAM. The bottlebrush architecture appears to disfavor non-lamellar morphologies, in spite of frustration favoring curved interfaces (*i.e.*, minimal A/B and B/C contacts). Chapter 4 reported our discovery of a unique partially mixed lamellar morphology (LAM_P) in select LSO triblocks. Partial mixing may allow compromises between the demands of the bottlebrush architecture and the enthalpic preference for A/C contacts. Transmission electron microscopy (TEM), self-consistent field theory (SCFT), and the unusual trend in the lamellar period with total molecular weight all provide compelling evidence that the reported LSO-N_C ($52 \leq N_{bb} \leq 70$) triblocks all assemble to LAM_P. We note however that the LSO-N_C series is not representative of all LAM materials in Figure 5.3. First, N_{bb} is shorter among the LSO-N_C series; second, whereas the composition window for LSO-N_C is narrow ($0.5 < f_{PLA} < 0.6$, $0.3 < f_{PS} < 0.4$), the LAM region spans a very wide range of compositions ($0.05 < f_{PLA} < 0.7$, $0.3 < f_{PS} < 0.7$). Whether all or merely some of the LAM materials identified in Figure 5.3 are LAM_P (rather than conventional unmixed LAM_2 or LAM_3) must be confirmed by TEM or additional X-ray scattering experiments.

Narrow regions of DIS and HEX appear in the ternary phase diagram as the volume fraction of PS decreases. HEX emerges when $f_{PS} \approx 0.25$. Partial mixing is likely, featuring minority PS cylinders in a matrix of PLA/PEO. When $f_{PS} \approx 0$ (*i.e.*, LSO resembles LO), the materials are disordered. This is consistent with the extremely low — potentially even negative — value of χ_{LO}. Actual literature estimates for χ_{LO} range from 0.0038 to −0.161 depending on end groups and measurement techniques.[35-36] In the previous chapter, we proposed that the magnitude of χ_{LO}, beyond simple frustration effects, drives the formation of LAM_P (Chapter 4-2 and 4-6). The consequences of low-χ design clearly also emerge in the full brush LSO phase diagram.

5-1.2 SLO and LOS Brush Triblock Terpolymers

In addition to brush LSO, we also synthesized and studied brush SLO and brush LOS triblock terpolymers. Changing the block sequence changes the type of morphological frustration imposed by the relative binary interaction parameters (Figure 5.4).[25] LSO features the lowest-χ interactions between the end blocks (χ_{LO}) and therefore Type II frustration. Switching the order of the first two blocks produces SLO triblock terpolymers with Type I frustration ($\chi_{AB} > \chi_{AC} > \chi_{BC}$), which favors end-block contacts over some but not all contacts between adjacent blocks. Lastly, the third unique permutation produces LOS triblock terpolymers that do not experience morphological frustration ($\chi_{AC} > \chi_{BC} > \chi_{AB}$).

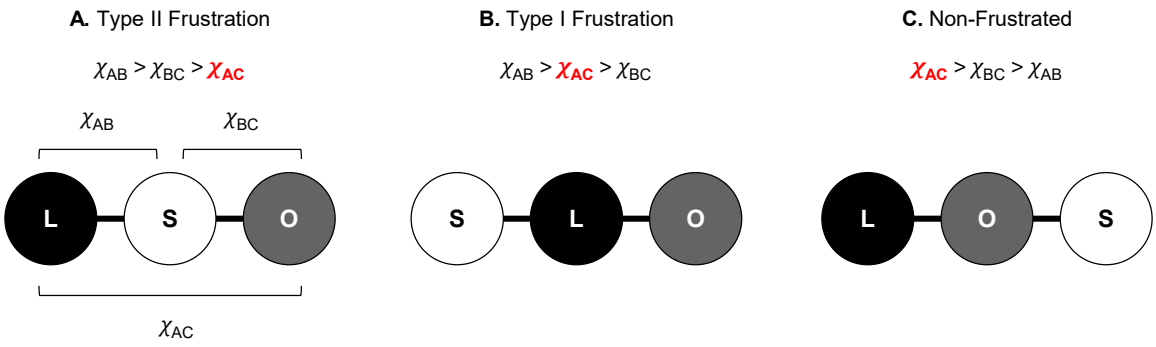

Figure 5.4: ABC triblock terpolymers can be classified according to the relative magnitude of χ_{AC}. (*A–C*) Each circle above represents a block, connected A-B-C from left to right. The contrast between circles represents the relative magnitude of χ; that is, black and white is the highest-contrast pair and therefore represents the highest-χ interaction in the system. (*A*) If χ_{AC} is the smallest interaction parameter, the system experiences Type II frustration. (*B*) If χ_{AC} is larger than one of, but not both, χ_{BC} and χ_{AB}, the system experiences Type I frustration. (*C*) If χ_{AC} is the largest interaction parameter, the system is non-frustrated.

SLO and LOS brush triblocks were synthesized by living ROMP. The total backbone degree of polymerization (N_{bb} = 80) and the side chain molecular weights were fixed, while the compositions were varied via the relative backbone lengths. All samples were thermally annealed and characterized by SAXS. The resulting ternary phase diagrams for brush SLO and brush LOS are provided in Figure 5.5A and 5.5 B, respectively. As for brush LSO, only HEX and LAM morphologies are observed, likely as a consequence of the extended bottlebrush architecture. However, because the PLA and PEO blocks are adjacent in SLO and LOS, partial PLA/PEO mixing (if any) may play a different role than in LSO.

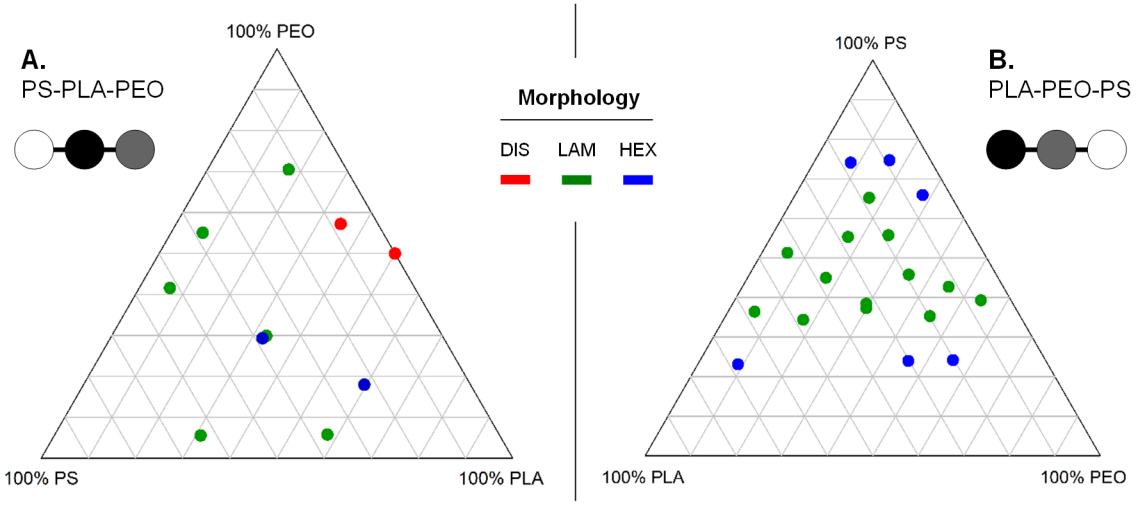

Figure 5.5: Ternary phase diagrams for (*A*) brush SLO and (*B*) brush LOS triblock terpolymers. The colors indicate different morphologies: (*red*) disordered, (*green*) lamellar, (*blue*) hexagonally packed cylinders.

Collectively, these studies of LSO, SOL, and LOS brush triblock terpolymers provide insights into the roles of molecular architecture and morphological frustration in block polymer self-assembly. Consistent with previous reports of related brush diblock polymers, the bottlebrush architecture appears to strongly favor lamellar morphologies: LAM is observed across wide swaths of the composition space (Figures 5.3 and 5.5), even at highly asymmetric compositions where analogous linear block polymers would assemble to 2D or 3D morphologies (Figures 5.1–5.2). This result reinforces a recurring theme of this thesis: namely, densely grafted brush polymers adopt rigid, extended conformations relative to their linear analogues. However, brush polymers should not be considered rigid rods: although the bending rigidity of the backbone appears to largely resist interfacial curvature in brush LSO, SOL, and LOS, exceptions emerge in the formation of HEX morphologies. Future work will perform complementary SAXS, TEM, and SCFT studies to expand our understanding of the dialogue between architecture and frustration in these materials.

5-2 Potential Non-Equilibrium Behavior

The preceding discussion assumes that equilibrium morphologies are attained for brush triblock terpolymers. Although SCFT calculations suggest that LAM$_P$ is at equilibrium with experimentally relevant values of χ and f, experimental proof is currently limited by our inability to access the order-disorder transition temperature (T_{ODT}). SAXS data obtained upon heating a LAM$_P$ sample (LSO with N_A = 25, N_B = 22, N_C = 5) from 25 to 200 °C indicate that LAM$_P$ is thermally stable throughout the entire experimentally accessible temperature range (Figure 5.6). Consistent with other reports of high-molar-mass bottlebrush polymers,[5,37] no T_{ODT} is observed below the onset of decomposition, preventing careful annealing and quench studies originating from the disordered state.

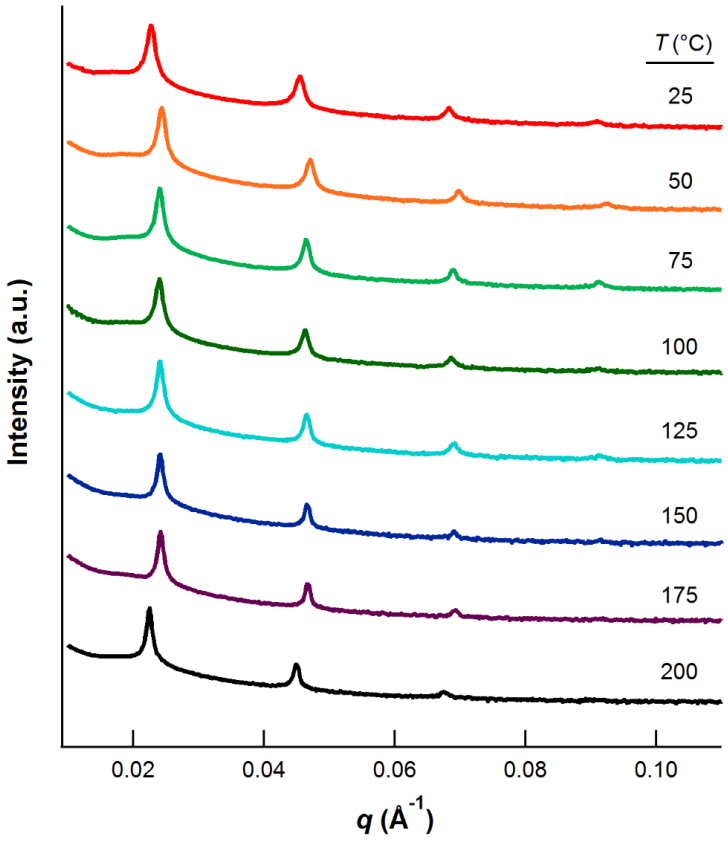

Figure 5.6: SAXS data for an LSO brush triblock terpolymer (N_A = 25, N_B = 22, N_C = 5) obtained upon heating from 25 to 200 °C at 1 °C/min. The lamellar morphology (LAM$_P$) is stable throughout the entire experimentally accessible temperature range. d^* varies slightly (<5%) over this range. No order-disorder transition is observed at any temperature below the onset of decomposition.

All LSO samples exhibit similar behavior, although low-molecular-weight samples suggest that non-equilibrium effects may in fact exist. When N_C is large (*e.g.*, LSO-14, Figure 5.7A), no significant changes are observed throughout the heating and cooling cycle. However, when N_C is short, additional peaks appear upon cooling that suggest minor higher-symmetry contributions (*e.g.*, LSO-4, Figure 5.7B). These N_C-dependent observations are consistent with at least some LSO samples exhibiting persistent metastability close to a phase boundary rather than true equilibrium.[38] Since SCFT is an equilibrium theory, such deviations from equilibrium would affect the agreement between experimentally measured results and predicted behavior.

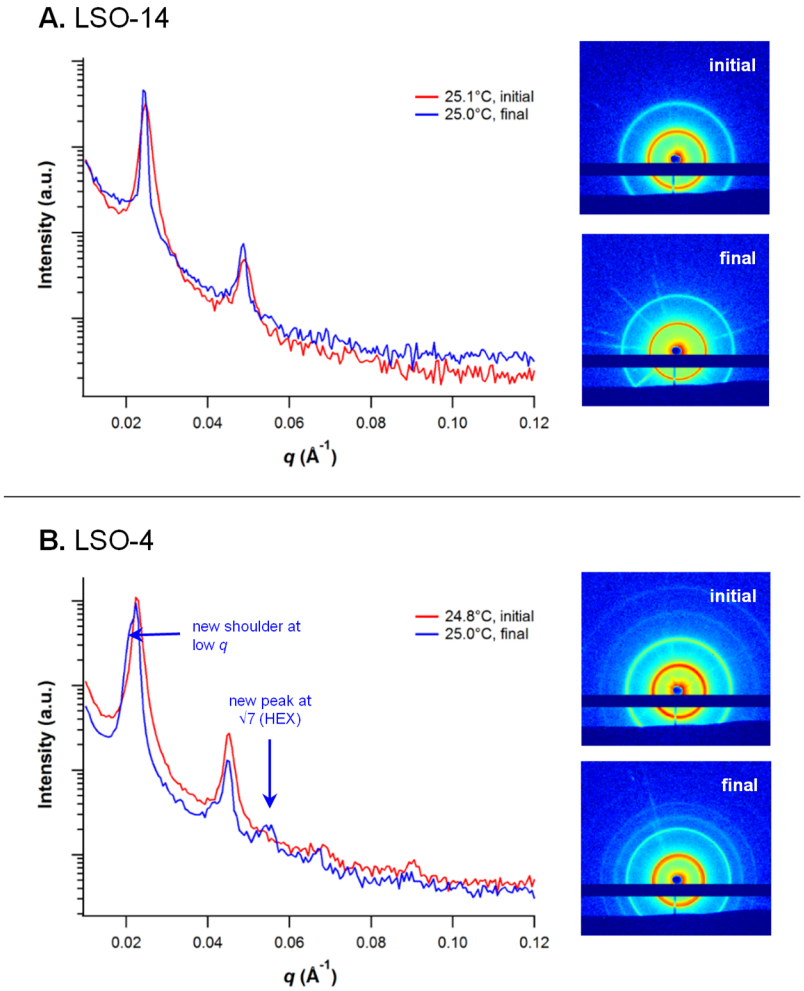

Figure 5.7: Variable-temperature SAXS measurements for (*A*) LSO-14 and (*B*) LSO-4. Samples were heated without pressure at 2 °C/min from 25 to 200 °C, then cooled back to 25 °C at 2 °C/min. Red and blue traces correspond to measurements before and after heating, respectively. (*A*) When N_C is long, the peaks become sharper on heating, but otherwise no changes are observed with temperature. (*B*) When N_C is short, features consistent with HEX emerge on heating.

To further examine potential non-equilibrium effects, because morphologies for multiblock polymers can be highly sensitive to processing conditions,[39-40] an LSO brush triblock terpolymer ($N_A = 25$, $N_B = 22$, $N_C = 5$) was annealed in four different ways: thermal annealing under pressure, thermal annealing without pressure, drop casting, and channel die alignment. All approaches afforded self-assembled morphologies with virtually identical LAM$_P$ geometry and periodicity (± 0.5 nm) (Figure 5.8). These results are reported while acknowledging studies of linear multiblock polymers that highlight the potential influence of processing path on the formation of kinetically trapped structures,[38,41] which may be mistaken for equilibrium. Previously, ABC block polymer morphologies containing partially mixed regions have indeed been predicted[20] and observed[42] as metastable defect states kinetically trapped upon casting from preferential solvents, but these examples were easily annihilated during the type of extended thermal treatments performed herein to anneal LSO. Equilibrium or not, the morphological attributes of LAM$_P$ are long-lived, in contrast to and notably distinct from prior materials.

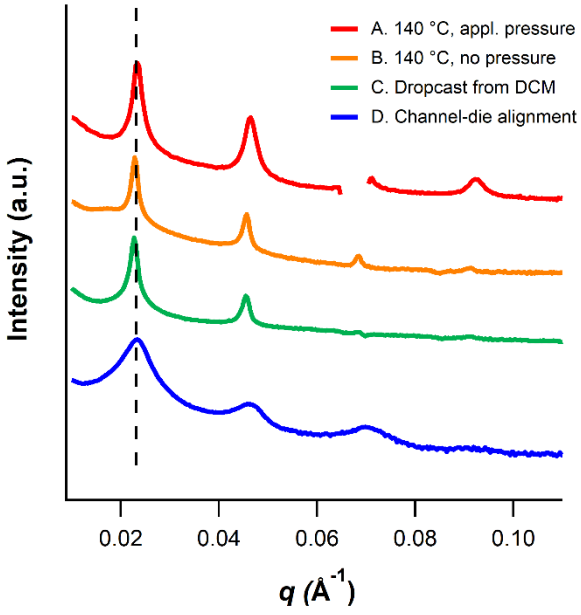

Figure 5.8: Azimuthally integrated 1D SAXS data for an LSO triblock terpolymer ($N_A = 25$, $N_B = 22$, $N_C = 5$) annealed in four different ways: (*A*) Thermally annealed at 140 °C between Kapton under modest applied pressure; (*B*) thermally annealed at 140 °C in a DSC pan with no applied pressure; (*C*) dropcast from DCM onto a glass cover slip; and (*D*) channel-die alignment at 140 °C. SAXS data corresponding to all methods indicate the same morphology (LAM) and period (± 0.5 nm). Note that the discontinuity at $q \approx 0.065$ Å^{-1} in (*A*) is due to a mask applied when averaging the raw 2D data.

5-3 Crystallization

5-3.1 Crystallization and Domain Spacing Trends

In the preceding chapter, we identified the screening of unfavorable PLA/PS contacts as the primary motivation for the unusual domain spacing trend observed in LSO-N_C brush triblock terpolymers. Due to preferential localization of PEO at the PLA/PS interface, when increasing backbone block lengths of PEO are installed from a parent LS diblock, the domain spacing *decreases* even though the total molecular weight increases. Chain pull-out due to molecular asymmetry is another potential factor (Chapter 4-7), but complementary resonant soft X-ray reflectivity (RSoXR) measurements and self-consistent field theory (SCFT) suggest that any chain pull-out effect is minor (Chapter 4-10). A third potential explanation for the unusual trend is crystallization, which we address in this section through wide-angle X-ray scattering (WAXS) measurements.

Little evidence of PEO crystallization is observed on the timescale of sample preparation and analysis. All characterization by SAXS was performed within three days of annealing. Variable-temperature WAXS measurements indicate that all LSO LAM_P samples contain low crystalline weight fractions (<10 wt%) (Figure 5.9). (Further information about WAXS experiments can be found in Appendix C-10.) Densification upon PEO crystallization and concomitant domain contraction is therefore unlikely. The higher-molecular-weight O blocks in linear poly(isoprene-*b*-styrene-*b*-ethylene oxide) (ISO) and poly(styrene-*b*-isoprene-*b*-ethylene oxide) (SIO) triblock terpolymers would presumably accentuate this effect, yet both ISO and SIO show strong increases in d^* with N_C (Chapter 4-5).[43-45] Comparing LSO and LSL' provides further evidence that crystallization is not responsible for the unusual trend in d^*: while both LSO and LSL' exhibit decreasing d^* with increasing end block lengths, LSL' has no crystallizable components.

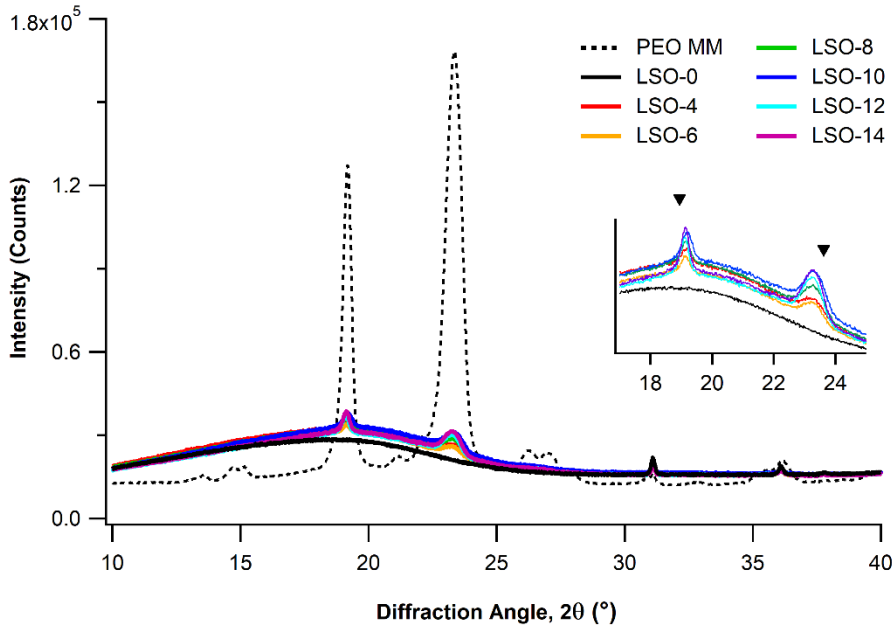

Figure 5.9: Wide-angle X-ray scattering (WAXS) data for the PEO macromonomer (MM, *i.e.,* linear PEO), brush PLA-PS parent diblock (LSO-0), and 6 selected LSO-N_C triblock terpolymers that self-assemble to LAM_P. (These data were obtained at 25°C; variable-temperature WAXS data is provided in Figure C.15.) Reflections at $2\theta = 19.1°$ and 23.2° for LSO-N_C (▼, inset) and PEO MM match the (120) and (032) reflections from a monoclinic PEO lattice.[46] The parent diblock (LSO-0), which contains no PEO, is amorphous as expected. Crystallization is suppressed in the LSO brush triblock terpolymers compared to neat PEO. (Note: Minor peaks at 31.1° and 36.1° are artifacts present in every sample due to the geometry of the stage.)

5-3.2 Crystallization Kinetics

Although little evidence of crystallization was observed three days after annealing, we note that the kinetics of crystallization are typically arrested in densely grafted brush polymers.[47-48] In order to assess the possibility that crystallization occurs over time, we performed synchrotron-source SAXS and WAXS measurements on the same LSO-N_C samples one year after the original measurements ($2 \leq N_C \leq 30$). The samples were stored at room temperature. The SAXS data collected both 3 days and 365 days after annealing are provided in Figure 5.10. WAXS data collected 365 days after annealing are also provided in Figure 5.10; however, since no evidence of crystallization was observed in any of the samples 3 days after annealing, the corresponding WAXS data are not included.

Figure 5.1 (Part 1/4): Raw 2D SAXS (*left, middle*) and WAXS (*right*) data for LSO-N_C brush triblock terpolymers. The same set of samples was measured either (*left*) 3 days after annealing or (*middle, right*) 365 days after annealing. N_C = (*A*) 2, (*B*) 4, (*C*) 6.

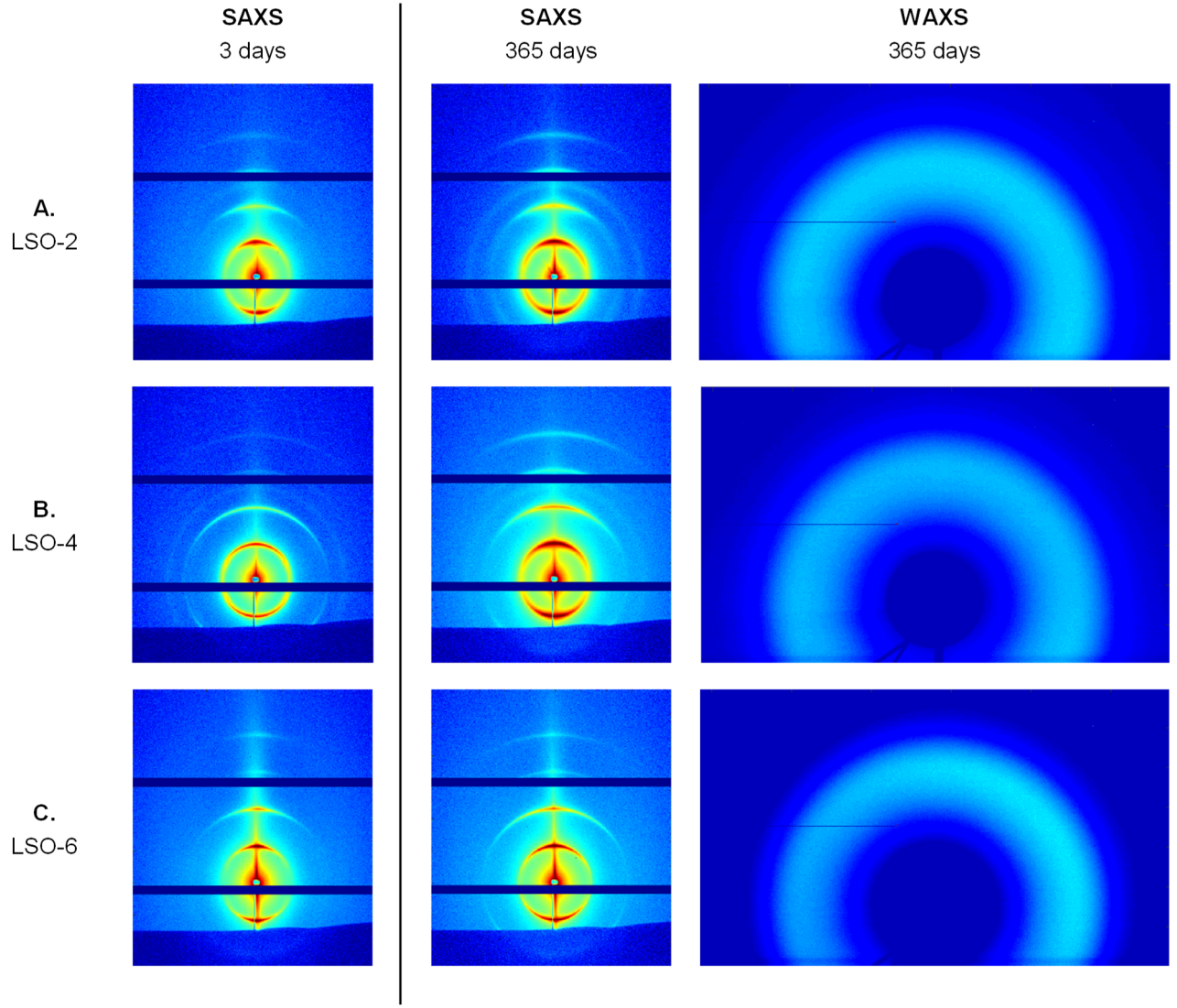

Figure 5.10 (Part 2/4): Raw 2D SAXS (*left, middle*) and WAXS (*right*) data for LSO-N_C brush triblock terpolymers. The same set of samples was measured either (*left*) 3 days after annealing or (*middle, right*) 365 days after annealing. N_C = (*D*) 8, (*E*) 10, (*F*) 12.

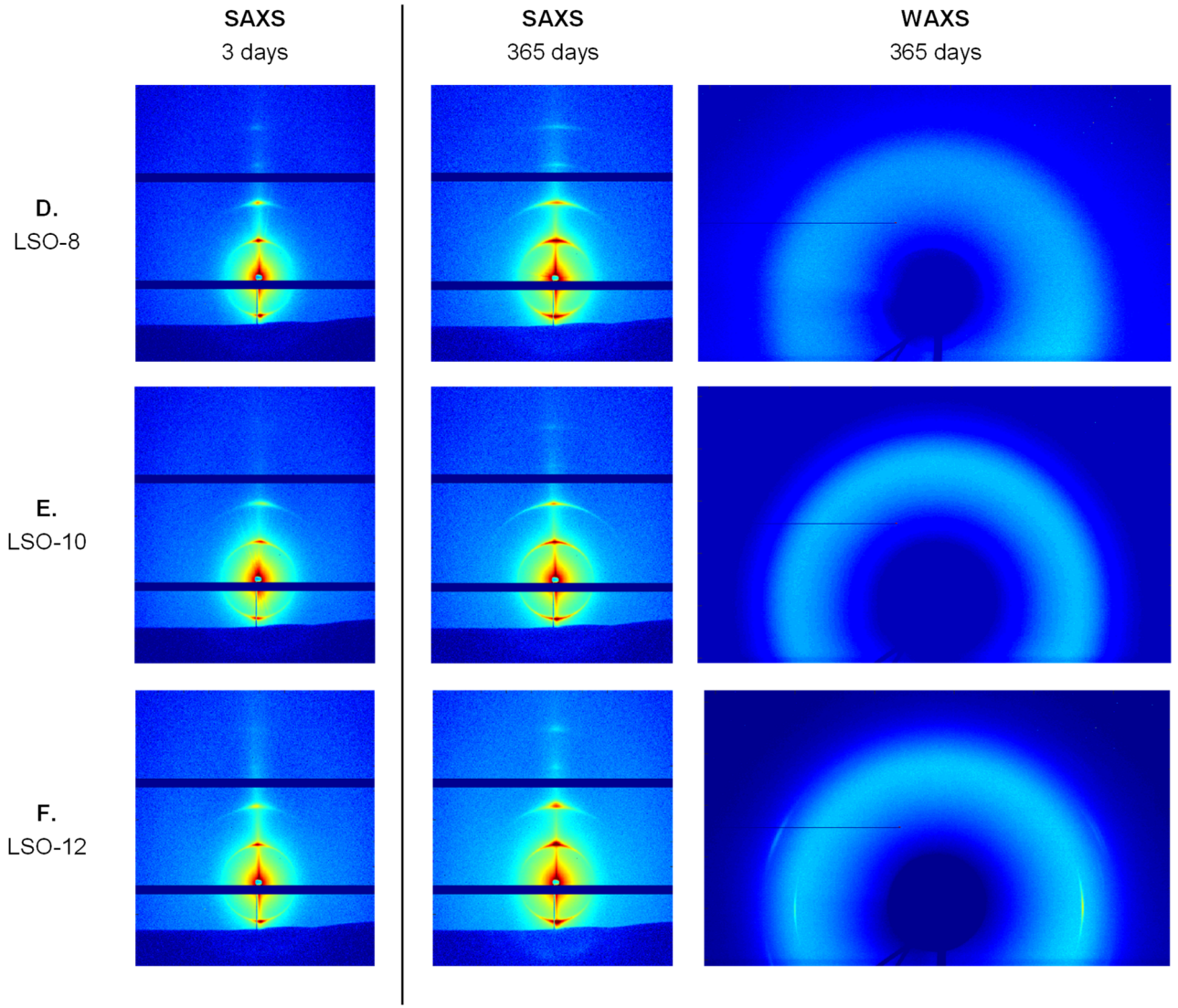

Figure 5.10 (Part 3/4): Raw 2D SAXS (*left, middle*) and WAXS (*right*) data for LSO-N_C brush triblock terpolymers. The same set of samples was measured either (*left*) 3 days after annealing or (*middle, right*) 365 days after annealing. N_C = (*G*) 14, (*H*) 16, (*I*) 20.

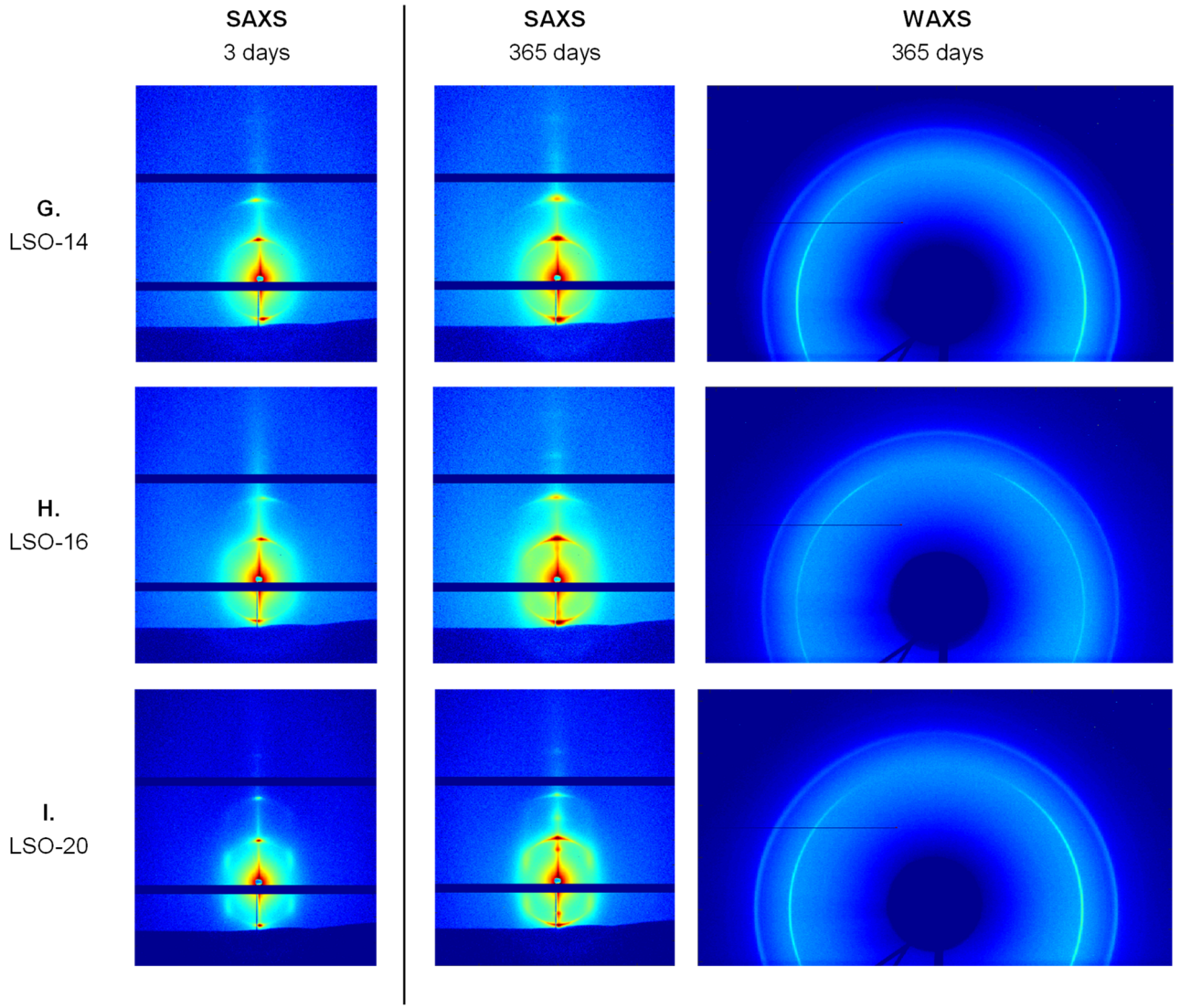

Figure 5.10 (Part 4/4): Raw 2D SAXS (*left, middle*) and WAXS (*right*) data for LSO-N_C brush triblock terpolymers. The same set of samples was measured either (*left*) 3 days after annealing or (*middle, right*) 365 days after annealing. N_C = (*J*) 24, (*K*) 26, (*L*) 30.

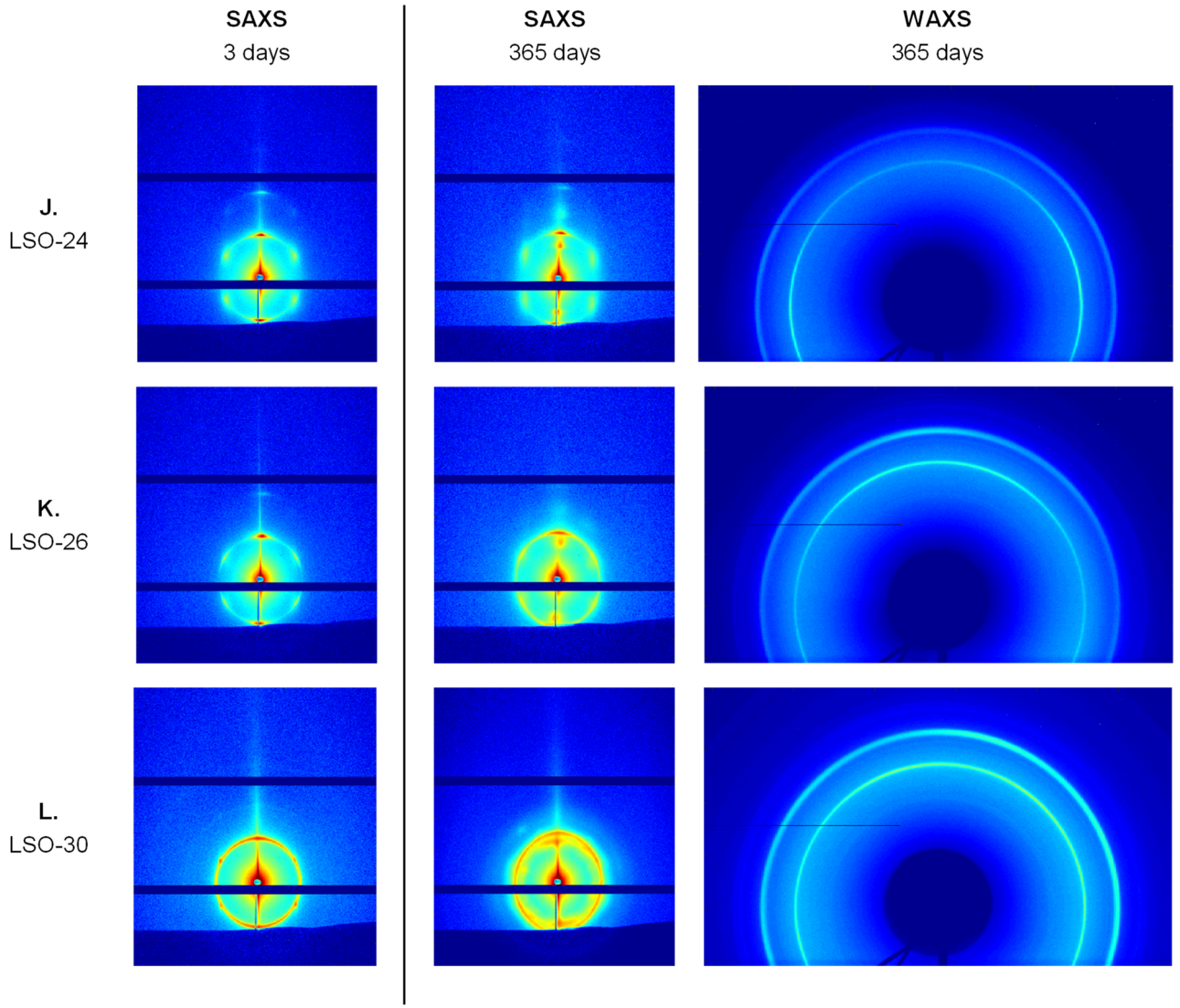

In the discussion of the SAXS and WAXS data presented in Figure 5.10, we will first discuss changes in the observed morphology over time, then comment on the onset of crystallization. We will then discuss potential confinement effects on the kinetics of crystallization. Lastly, we will interpret the orientation of PEO crystals in terms of confinement and the backbone orientation.

The SAXS data in Figure 5.10 indicate that, after aging for one year, each LSO-N_C sample generally retained its initial geometry: that is, LAM$_P$ samples were still lamellar ($2 \leq N_C \leq 16$, Figure 5.10A–H), and samples that had HEX character ($20 \leq N_C \leq 30$, Figure 5.10I–L) still display HEX features. (We note that a new low-q peak appears for these HEX samples. TEM and additional X-ray scattering experiments are underway to confirm the morphology.) However, for samples with relatively long backbone lengths of the PEO block ($N_C \geq 14$), the domain spacing monotonically *decreases* as N_C increases. The values of d^* after one year, normalized to their values measured 3 days after annealing, are provided in Figure 5.11. We emphasize that this behavior is distinct from the unusual domain spacing trend identified in Chapter 4, since it manifests long after the initial data collection and analysis.

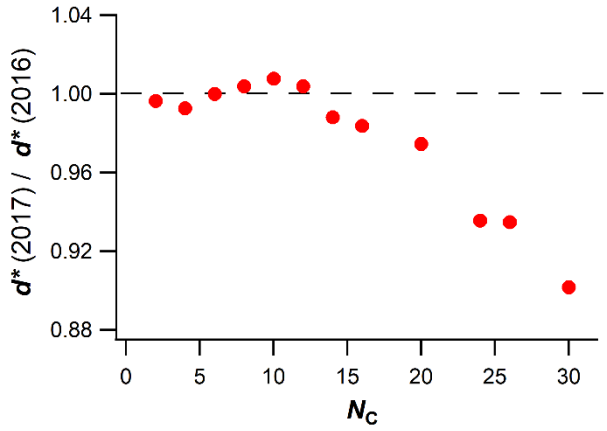

Figure 5.11: Changes in d^* over one year (2016–2017). $d^*(2017)/d^*(2016)$ is the ratio of d^* measured by SAXS 365 days after annealing and d^* measured 3 days after annealing. When the backbone length of the PEO block is short ($N_C \leq 12$), no significant change in d^* is observed over time. However, when N_C is long ($N_C \geq 14$), d^* decreases, concomitant with crystallization of the O blocks observed by WAXS.

The WAXS data indicate that the decrease in d^* is concomitant with the crystallization of PEO blocks. The azimuthally averaged WAXS data are provided in Figure 5.12. Peaks consistent with the (120) and ($\bar{1}32, 032, \bar{2}12, 112$) reflections of PEO crystals are observed for all LSO samples with $N_C \geq 14$ (at q = 1.36 and 1.67 Å^{-1}, respectively). These peaks can also be observed in the 2D WAXS data for LSO-12 (Figure 5.10F) but cannot be clearly distinguished in the 1D reduction because the peaks are relatively low-intensity compared to the amorphous scattering.

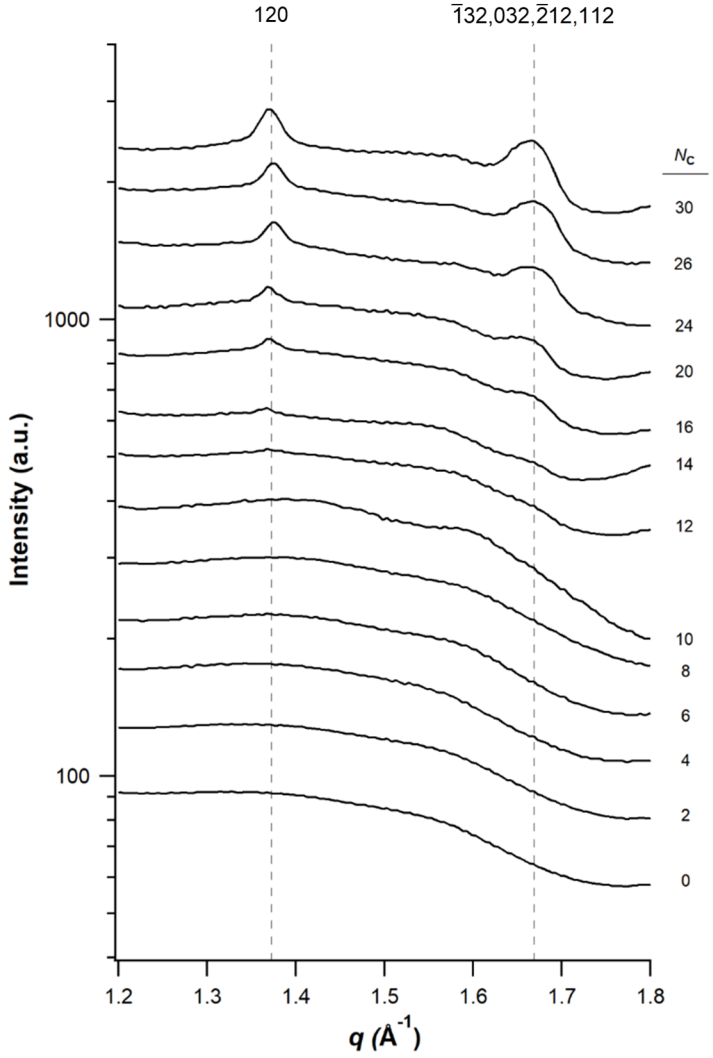

Figure 5.12: Azimuthally averaged 1D WAXS data for LSO-N_C, measured 365 days after annealing. Reflections consistent with PEO crystals are observed for $N_C \geq 14$ (120 at q = 1.36 Å^{-1}; $\bar{1}32, 032, \bar{2}12, 112$ at q = 1.67 Å^{-1}). Traces have been shifted vertically for clarity.

There are three potential factors influencing the slow kinetics of crystallization in brush LSO: the bottlebrush architecture, PLA/PEO mixing, and confinement. First, densely grafted brushes generally exhibit arrested crystallization kinetics. This influence will be discussed further in Chapter 6-2 in the context of PEO-containing electrolyte materials. Second, in the LAM_P morphology, the PLA and PEO end blocks are partially mixed. In order to form crystals, PEO blocks must be expelled from the mixed PLA/PEO phase. Depending on N_C, the mixed phase may be glassy at room temperature. The glass transition temperature (T_g) of the mixed phase monotonically decreases with increasing N_C, from 53 °C ($N_C = 2$) to 3 °C ($N_C = 30$). The observed onset of crystallization at $N_C = 12$ after one year may be influenced by the value of T_g near room temperature ($T_g = 30$ °C); for samples with $T_g > 30$ °C, the kinetic barrier to demixing PEO from the PLA/PEO phase may prevent crystallization. Confined crystallization is a third important factor to consider.

5-3.3 Confined Crystallization and Chain Orientation

Three competing events determine the final morphology in amorphous-semicrystalline block polymers: microphase separation in the melt (T_{ODT}), crystallization of the crystallizable block (T_c), and vitrification of the amorphous block (T_g).[49-51] The values of T_{ODT}, T_c, and T_g determine the type of confinement: (1) hard confinement ($T_{ODT} > T_g > T_c$); (2) soft confinement ($T_{ODT} > T_c > T_g$); and (3) crystallization-induced microphase separation ($T_{ODT} < T_c$, $T_g < T_c$) (Figure 5.13).

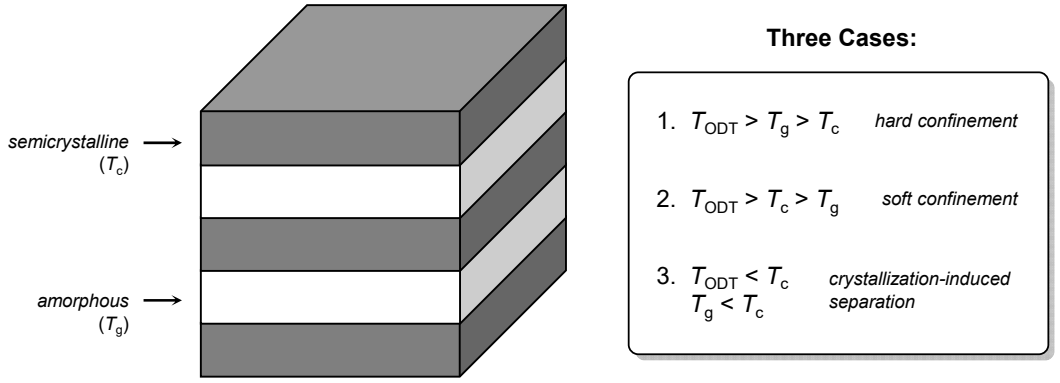

Figure 5.13: Potential types of confined crystallization in the self-assembly of block polymers with one amorphous block and one semicrystalline block. The glass transition temperature (T_g) of the amorphous block, together with the crystallization temperature (T_c) of the crystallizable block, determine three cases for confinement (*right*): hard, soft, and crystallization-induced microphase separation.

In the LSO system, T_{ODT} is thermally inaccessible but is at least greater than 200 °C (Figure 5.6). The T_g values of both amorphous blocks are high ($T_{g,PLA}$ = 55 °C, $T_{g,PS}$ = 100 °C) compared to the T_c of the crystallizable block (PEO, T_c = 20 °C). This combination of relevant parameters indicates that crystallization of PEO in LSO triblock terpolymers occurs under hard confinement, strictly bounded by glassy PS domains. For similar reported PEO-containing block polymers, PEO crystallization is significantly slower under hard confinement than under soft confinement or in the absence of confinement.[52] In addition to the brush architecture and barrier to PLA/PEO demixing, confinement effects potentially contribute to the slow crystallization kinetics of brush LSO.

Depending on the bulk geometry and the domain sizes, confinement can also influence the orientation of crystals.[51,53] The lamellar morphology is the simplest confining geometry (Figure 5.14A). The 2D WAXS pattern for LSO-12 indicates that the PEO crystals are remarkably oriented (Figure 5.10F). In fact, the data closely resembles the *fiber* diffraction pattern for PEO crystals (Figure 5.12B).[51] Comparison of the 2D WAXS patterns for all LSO-N_C samples indicates that the orientation of the crystals changes as N_C increases.

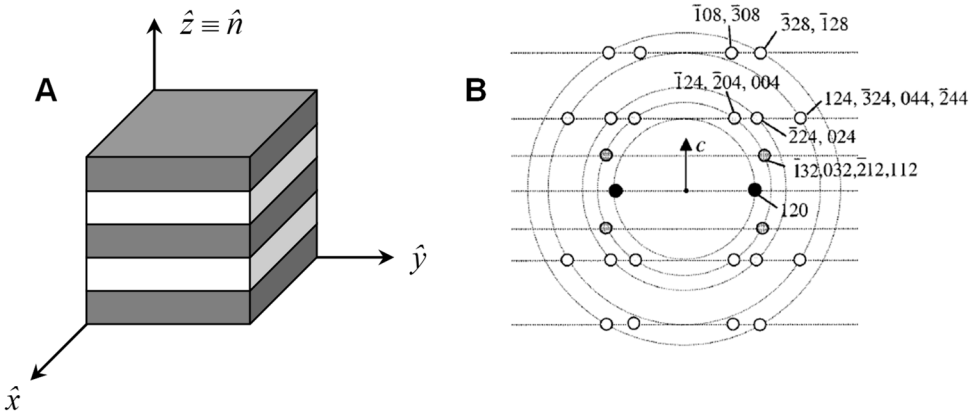

Figure 5.14: (*A*) Geometry of the wide-angle X-ray scattering stage. The lamellar normal $\hat{n}$ is parallel to $\hat{z}$ and perpendicular to the $\hat{x}-\hat{y}$ plane. Samples were measured with the X-ray beam along $\hat{x}$. (*B*) Fiber pattern of PEO crystals, constructed by rotating the reciprocal lattice along the *c*-axis. Adapted from Ref. 51 with permission from the American Chemical Society.

For confined crystallization in a lamellar geometry, two extremes of chain orientations exist with respect to the lamellar normal ($\hat{n}$). The chain direction (typically the crystal *c*-axis) can be oriented either parallel (homeotropic, Figure 5.15A) or perpendicular

(homogeneous, Figure 5.15B) to $\hat{n}$. In the absence of confinement, the crystals typically exhibit no preferential orientation (Figure 5.15C). The homeotropic PEO crystal orientation has been proposed to be the most thermodynamically stable configuration, and it has been identified in various PEO-containing linear block polymers crystallized from dilute solution, including PEO-*b*-PS,[54] PEO-*b*-polyisoprene (PI),[55] and PEO-*b*-poly(butylene oxide) (PBO).[56] In contrast, the homogeneous crystal orientation is rare; most observations have been made for shear-aligned polyethylene-containing block polymers.[57-59]

The 2D WAXS pattern for LSO-12 is consistent with a homeotropic crystal orientation. This chain orientation for the PEO side chains strongly suggests that the brush backbone is oriented perpendicular to $\hat{n}$; that is, the PEO crystal orientation suggests that the backbone is highly oriented *parallel* to the PLA/PS domain interface (Figure 5.16A). The 2D WAXS images in Figure 5.10 indicate that, as the PEO backbone length increases to N_C = 24, the extent of orientation decreases but the PEO crystals generally remain homeotropically oriented. However, when N_C = 26, WAXS data suggests that the orientation switches, such that PEO crystals favor the homogeneous orientation and the brush backbones are aligned *perpendicular* to the PLA/PS domain interface (Figure 5.16B). Upon increasing to N_C = 30, the crystal orientation is isotropic, consistent with the observation of a HEX morphology by SAXS (Figure 5.16C).

The WAXS data suggests that the PEO block backbone in LSO-12 is strongly oriented *parallel* to the domain interface, introducing extreme bending at the block-block junction (Figure 5.16A). This observation is at first surprising, especially in the context of the discussion in Chapter 5-1, which indicates that the bottlebrush architecture generally disfavors to interfacial curvature. However, we note that significant backbone bending in brush LSO has been confirmed via the existence of looping PS midblocks (Chapter 4-10). Screening — the underlying physical motivation for backbone bending to form PS loops — likely also motivates the backbone bending inferred in crystalline LSO-12. Orienting the PEO block backbone parallel to the PLA/PS interface maximizes the number of PLA/PEO and PS/PEO contacts. The onset of crystallization would “lock in” this backbone orientation, resulting in a homeotropic crystal orientation. In turn, the homeotropic crystal orientation is thermodynamically favorable since it permits the growth of crystals parallel to the domain

interface and therefore maximizes the possible crystallite size. However, as N_C increases, the entropic penalty to aligning the brush backbone along the interface may overwhelm the enthalpic screening advantages, resulting in the gradual loss of the homeotropic crystal orientation and eventually a transition to the homogeneous crystal orientation (Figure 5.16B).

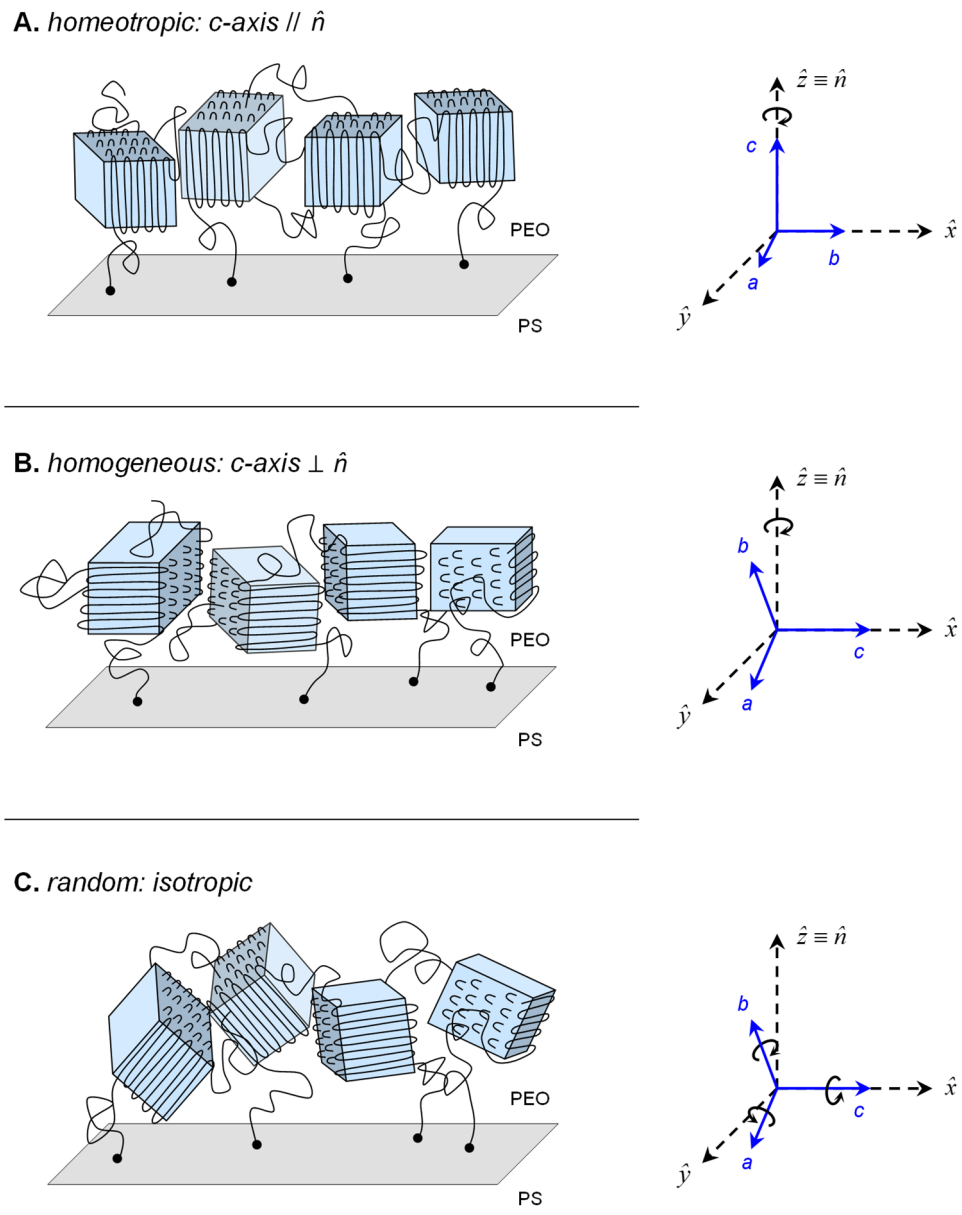

Figure 5.15: Schematic illustrations of orientations of PEO crystallites with respect to the lamellar normal, $\hat{n}$. The X-ray beam is along $\hat{x}$, and the gray planes represent the interface between PLA/PEO and PS domains. (*A*) Homeotropic alignment: the *c*-axis of the crystals is parallel to $\hat{n}$. (*B*) Homogeneous alignment: the *c*-axis is perpendicular to $\hat{n}$. (*C*) Random: no preferred orientation is observed.

Figure 5.16: Comparison of the (*left*) 2D WAXS data along $\hat{x}$, (*middle*) PEO crystal orientation, and (*right*) inferred brush backbone orientation. (*A*) $N_C = 12$: homeotropic alignment is observed. $c \,//\, \hat{n}$ suggests that the PEO block backbone is orthogonal to $\hat{n}$. (*B*) $N_C = 26$: homogeneous alignment is observed. $c \perp \hat{n}$ suggests that the PEO block backbone is parallel to $\hat{n}$. (*C*) $N_C = 30$: random orientations are observed, consistent with the HEX morphology identified by SAXS.

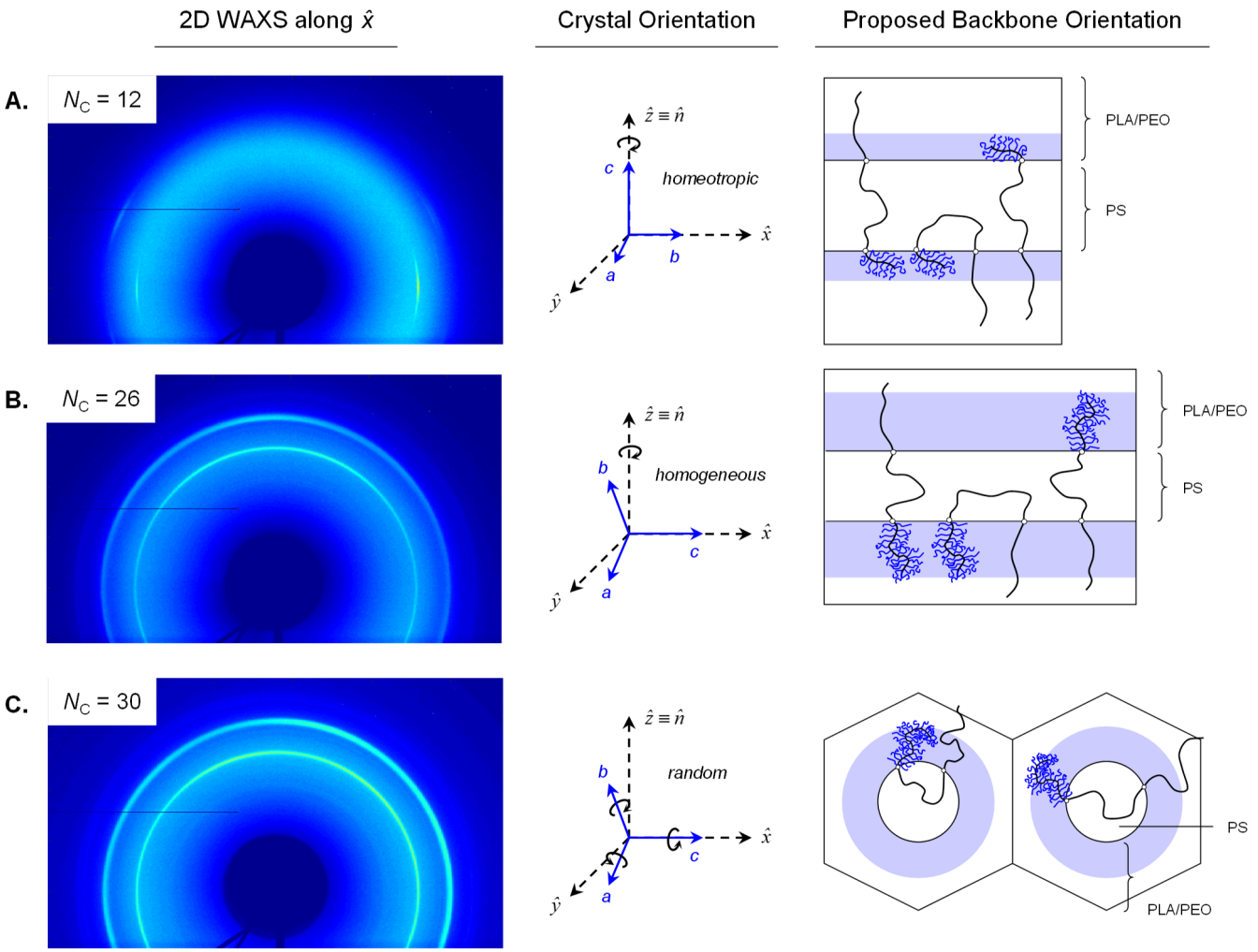

The crystallization of PEO in brush LSO triblock terpolymers reveals rich connections between the polymer dynamics, low-χ interactions, and chain orientation. Little evidence of crystallization was observed within several days of annealing, but after aging the samples at room temperature for one year, crystallization was observed for certain samples ($N_C \geq 12$). The arrested crystallization kinetics in brush LSO reflect the interplay of the bottlebrush architecture, PLA/PEO demixing, and hard confinement effects. Confinement leads to orientation of the PEO crystals — and therefore the brush backbone — with respect to the lamellar geometry. To initial surprise, the crystal orientation suggests extreme backbone bending for short N_C. As described herein and in Chapter 4, low-χ interactions drive this unusual behavior, thereby overcoming the bending rigidity introduced by the bottlebrush architecture.

5-4 References

(1) Kikuchi, M.; Nakano, R.; Jinbo, Y.; Saito, Y.; Ohno, S.; Togashi, D.; Enomoto, K.; Narumi, A.; Haba, O.; Kawaguchi, S. *Macromolecules* **2015**, *48*, 5878–5886.
(2) Liang, H.; Cao, Z.; Wang, Z.; Sheiko, S. S.; Dobrynin, A. V. *Macromolecules* **2017**, *50*, 3430–3437.
(3) Paturej, J.; Sheiko, S. S.; Panyukov, S.; Rubinstein, M. *Sci. Adv.* **2016**, *2*, e1601478.
(4) Rathgeber, S.; Pakula, T.; Wilk, A.; Matyjaszewski, K.; Beers, K. L. *J. Chem. Phys.* **2005**, *122*, 124904.
(5) Xia, Y.; Olsen, B. D.; Kornfield, J. A.; Grubbs, R. H. *J. Am. Chem. Soc.* **2009**, *131*, 18525–18532.
(6) Rzayev, J. *Macromolecules* **2009**, *42*, 2135–2141.
(7) Sveinbjörnsson, B. R.; Weitekamp, R. A.; Miyake, G. M.; Xia, Y.; Atwater, H. A.; Grubbs, R. H. *Proc. Natl. Acad. Sci. U.S.A.* **2012**, *109*, 14332–14336.
(8) Song, D.-P.; Li, C.; Colella, N. S.; Xie, W.; Li, S.; Lu, X.; Gido, S.; Lee, J.-H.; Watkins, J. J. *J. Am. Chem. Soc.* **2015**, *137*, 12510–12513.
(9) Sveinbjörnsson, B. R. Self-Assembly of Brush Polymers. California Institute of Technology, 2014.
(10) Bates, F. S.; Fredrickson, G. H. *Annu. Rev. Phys. Chem.* **1990**, *41*, 525–557.
(11) Bates, F. S.; Fredrickson, G. H. *Phys. Today* **1999**, *52*, 32–38.
(12) Bolton, J.; Rzayev, J. *Macromolecules* **2014**, *47*, 2864–2874.
(13) Gai, Y.; Song, D.-P.; Yavitt, B. M.; Watkins, J. J. *Macromolecules* **2017**, *50*, 1503–1511.
(14) Runge, M. B.; Bowden, N. B. *J. Am. Chem. Soc.* **2007**, *129*, 10551–10560.
(15) Runge, M. B.; Lipscomb, C. E.; Ditzler, L. R.; Mahanthappa, M. K.; Tivanski, A. V.; Bowden, N. B. *Macromolecules* **2008**, *41*, 7687–7694.

(16) Kawamoto, K.; Zhong, M.; Gadelrab, K. R.; Cheng, L.-C.; Ross, C. A.; Alexander-Katz, A.; Johnson, J. A. *J. Am. Chem. Soc.* **2016**, *138*, 11501–11504.
(17) Zheng, W.; Wang, Z.-G. *Macromolecules* **1995**, *28*, 7215–7223.
(18) Kane, L.; Spontak, R. J. *Macromolecules* **1994**, *27*, 1267–1273.
(19) Bohbot-Raviv, Y.; Wang, Z.-G. *Phys. Rev. Lett.* **2000**, *85*, 3428–3431.
(20) Xia, J.; Sun, M.; Qiu, F.; Zhang, H.; Yang, Y. *Macromolecules* **2005**, *38*, 9324–9332.
(21) Tyler, C. A.; Qin, J.; Bates, F. S.; Morse, D. C. *Macromolecules* **2007**, *40*, 4654–4668.
(22) Liu, M.; Li, W.; Qiu, F.; Shi, A.-C. *Macromolecules* **2012**, *45*, 9522–9530.
(23) Auschra, C.; Stadler, R. *Macromolecules* **1993**, *26*, 2171–2174.
(24) Stadler, R.; Auschra, C.; Beckmann, J.; Krappe, U.; Voight-Martin, I.; Leibler, L. *Macromolecules* **1995**, *28*, 3080–3097.
(25) Bailey, T. S. Morphological behavior spanning the symmetric AB and ABC block copolymer states. University of Minnesota, 2001.
(26) Epps, T. H.; Cochran, E. W.; Bailey, T. S.; Waletzko, R. S.; Hardy, C. M.; Bates, F. S. *Macromolecules* **2004**, *37*, 8325–8341.
(27) Radlauer, M. R.; Sinturel, C.; Asai, Y.; Arora, A.; Bates, F. S.; Dorfman, K. D.; Hillmyer, M. A. *Macromolecules* **2016**, *50*, 446–458.
(28) Kumar, R.; Sides, S. W.; Goswami, M.; Sumpter, B. G.; Hong, K.; Wu, X.; Russell, T. P.; Gido, S. P.; Misichronis, K.; Rangou, S.; Avgeropoulos, A.; Tsoukatos, T.; Hadjichristidis, N.; Beyer, F. L.; Mays, J. W. *Langmuir* **2013**, *29*, 1995–2006.
(29) Krappe, U.; Stadler, R.; Voigt-Martin, I. *Macromolecules* **1995**, *28*, 4558–4561.
(30) Breiner, U.; Krappe, U.; Jakob, T.; Abetz, V.; Stadler, R. *Polym. Bull.* **1998**, *40*, 219–226.
(31) Brinkmann, S.; Stadler, R.; Thomas, E. L. *Macromolecules* **1998**, *31*, 6566–6572.
(32) Breiner, U.; Krappe, U.; Thomas, E. L.; Stadler, R. *Macromolecules* **1998**, *31*, 135–141.
(33) Breiner, U.; Krappe, U.; Stadler, R. *Macromol. Rapid Commun.* **1996**, *17*, 567–575.
(34) Ott, H.; Abetz, V.; Altstädt, V. *Macromolecules* **2001**, *34*, 2121–2128.
(35) Mao, H.; Hillmyer, M. A. *Macromol. Chem. Phys.* **2008**, *209*, 1647–1656.
(36) Lai, W.-C.; Liau, W.-B.; Lin, T.-T. *Polymer* **2004**, *45*, 3073–3080.
(37) Dalsin, S. J.; Rions-Maehren, T. G.; Beam, M. D.; Bates, F. S.; Hillmyer, M. A.; Matsen, M. W. *ACS Nano* **2015**, *9*, 12233–12245.
(38) Lipic, P. M.; Bates, F. S.; Matsen, M. W. *J. Polym. Sci., Part B: Polym. Phys.* **1999**, *37*, 2229–2238.
(39) Mori, K.; Hasegawa, H.; Hashimoto, T. *Polymer* **1990**, *31*, 2368–2376.
(40) Lodge, T. P.; Pudil, B.; Hanley, K. J. *Macromolecules* **2002**, *35*, 4707–4717.
(41) Chanpuriya, S.; Kim, K.; Zhang, J.; Lee, S.; Arora, A.; Dorfman, K. D.; Delaney, K. T.; Fredrickson, G. H.; Bates, F. S. *ACS Nano* **2016**, *10*, 4961–4972.
(42) Corté, L.; Yamauchi, K.; Court, F.; Cloître, M.; Hashimoto, T.; Leibler, L. *Macromolecules* **2003**, *36*, 7695–7706.
(43) Bailey, T. S.; Hardy, C. M.; Epps, T. H.; Bates, F. S. *Macromolecules* **2002**, *35*, 7007–7017.
(44) Meuler, A. J.; Ellison, C. J.; Qin, J.; Evans, C. M.; Hillmyer, M. A.; Bates, F. S. *J. Chem. Phys.* **2009**, *130*, 234903.

(45) Bailey, T. S.; Pham, H. D.; Bates, F. S. *Macromolecules* **2001**, *34*, 6994–7008.
(46) Takahashi, Y.; Tadokoro, H. *Macromolecules* **1973**, *6*, 672–675.
(47) Zhao, C.; Wu, D.; Huang, N.; Zhao, H. *J. Polym. Sci., Part B: Polym. Phys.* **2008**, *46*, 589–598.
(48) Bates, C. M.; Chang, A. B.; Momčilović, N.; Jones, S. C.; Grubbs, R. H. *Macromolecules* **2015**, *48*, 4967–4973.
(49) Loo, Y.-L.; Register, R. A.; Ryan, A. J. *Macromolecules* **2002**, *35*, 2365–2374.
(50) Schmalz, H.; Knoll, A.; Müller, A. J.; Abetz, V. *Macromolecules* **2002**, *35*, 10004–10013.
(51) Zhu, L.; Cheng, S. Z. D.; Calhoun, B. H.; Ge, Q.; Quirk, R. P.; Thomas, E. L.; Hsiao, B. S.; Yeh, F.; Lotz, B. *J. Am. Chem. Soc.* **2000**, *122*, 5957–5967.
(52) Zhu, L.; Mimnaugh, B. R.; Ge, Q.; Quirk, R. P.; Cheng, S. Z. D.; Thomas, E. L.; Lotz, B.; Hsiao, B. S.; Yeh, F.; Liu, L. *Polymer* **2001**, *42*, 9121–9131.
(53) Huang, P.; Zhu, L.; Guo, Y.; Ge, Q.; Jing, A. J.; Chen, W. Y.; Quirk, R. P.; Cheng, S. Z. D.; Thomas, E. L.; Lotz, B.; Hsiao, B. S.; Avila-Orta, C. A.; Sics, I. *Macromolecules* **2004**, *37*, 3689–3698.
(54) Lotz, B.; Kovacs, A. J.; Bassett, G. A.; Keller, A. *Kolloid-Z.u.Z.Polymere* **1966**, *209*, 115–128.
(55) Hirata, E.; Ijitsu, T.; Soen, T.; Hashimoto, T.; Kawai, H. *Polymer* **1975**, *16*, 249–260.
(56) Yang, Y.-W.; Tanodekaew, S.; Mai, S.-M.; Booth, C.; Ryan, A. J.; Bras, W.; Viras, K. *Macromolecules* **1995**, *28*, 6029–6041.
(57) Cohen, R. E.; Bellare, A.; Drzewinski, M. A. *Macromolecules* **1994**, *27*, 2321–2323.
(58) Hamley, I. W.; Patrick, J.; Fairclough, A.; Ryan, A. J.; Bates, F. S.; Towns-Andrews, E. *Polymer* **1996**, *37*, 4425–4429.
(59) Hamley, I. W.; Fairclough, J. P. A.; Terrill, N. J.; Ryan, A. J.; Lipic, P. M.; Bates, F. S.; Towns-Andrews, E. *Macromolecules* **1996**, *29*, 8835–8843.